

Half-quantized anomalous Hall effect in magnetic axion insulator

$\text{MnBi}_2\text{Te}_4/(\text{Bi}_2\text{Te}_3)_n$

Mingqiang Gu¹, Jiayu Li¹, Hongyi Sun¹, Yufei Zhao¹, Chang Liu¹, Jianpeng Liu^{2,4*} and Qihang Liu^{1,3,*}

¹*Shenzhen Institute for Quantum Science and Engineering (SIQSE) and Department of Physics, Southern University of Science and Technology, Shenzhen 518055, China*

²*School of Physical Science and Technology, ShanghaiTech University, Shanghai, 200031, China*

³*Guangdong Provincial Key Laboratory for Computational Science and Material Design, Southern University of Science and Technology, Shenzhen 518055, China*

⁴*ShanghaiTech laboratory for topological physics, ShanghaiTech University, Shanghai, 200031, China*

M. G. and J. L. contributed equally to this work.

*Emails: liujp@shanghaitech.edu.cn; liuqh@sustech.edu.cn

Abstract

The rising of topological materials $\text{MnBi}_2\text{Te}_4/(\text{Bi}_2\text{Te}_3)_n$ with built-in magnetization provides a great platform for the realization of long-sought axion insulators with time-reversal symmetry breaking. As the direct evidence of the quantized bulk magnetoelectric coupling, half-quantized anomalous Hall effect at the gapped surface has been predicted in axion insulators based on simplified models, yet to be realized. Using both model Hamiltonian and first-principles calculations, we demonstrate that by tailoring the magnetization and interlayer electron hopping, a rich three-dimensional topological phase diagram can be established based on $\text{MnBi}_2\text{Te}_4/(\text{Bi}_2\text{Te}_3)_n$ systems. It includes three types of topologically distinct insulating phases bridged by a Weyl semimetal phase. Among them, we find that the surface anomalous Hall conductivity in the axion-insulator phase is a well-localized quantity either saturated at or oscillating around $e^2/2h$, depending on the magnetic homogeneity. With the discussion of the experimental prerequisites and proposals, our study is a significant step forward towards the realization of half-quantized surface anomalous Hall effect in realistic material systems.

Three-dimensional (3D) crystalline insulators with non-vanishing Chern-Simons orbital magnetoelectric coupling exhibits effective axion electrodynamics, which are characterized by fractionalized surface anomalous Hall effect [1-4]. If either time-reversal (T) or inversion symmetry (I) is present, the coupling phase angle θ must be quantized as 0 or π (modulo 2π), the latter of which with an energy gap at the surface is also known as “axion insulators” [1,2,5]. Thus, the axion insulator exhibits quantized bulk magnetoelectric coupling coefficient, which is equivalent to a half-quantized surface anomalous Hall conductivity (AHC) $e^2/2h$. For 3D T -preserved topological insulators (TIs), however, such a half-quantized surface AHC is exactly compensated by the gapless surface Dirac cones of TIs. Therefore, the realization of the axion insulator phase was typically based on introducing extrinsic magnetic dopants to the top and bottom surfaces of a 3D TI to gap the surface states [6-9]. In a magnetic hysteresis loop, this setup would give rise to two quantum anomalous Hall states with opposite Chern numbers connected by an intermediate insulating phase with zero Hall plateau [10]. Compared with the quantum anomalous Hall state where the topological nature is well established by a nonzero Chern number and chiral edge states, the direct evidences of an axion insulator, such as the topological magnetoelectric effect and half quantization of the surface AHC, are much more challenging to measure [11,12].

The recent discovery of superlattice-like compounds $\text{MnBi}_2\text{Te}_4/(\text{Bi}_2\text{Te}_3)_n$ with Van der Waals (VdW) layer-stacking structures [13-18] presents a series of stoichiometric magnetic topological materials with fruitful topological phases, such as Chern insulator, quantum spin Hall (QSH) insulator, high-order TI, and axion insulator [19-25]. Among them, quantum anomalous Hall effect has been experimentally confirmed in odd-layer antiferromagnetic (AFM) MnBi_2Te_4 [19]. Zero Hall plateau is also observed in even-layer MnBi_2Te_4 as an indirect evidence of the axion insulator phase [20], which may exhibit half-quantized surface AHC. However, despite being a fascinating theoretical concept, some key issues about the half-quantized surface AHC in this material family, such as the locality and the device design, still remain elusive.

In this Letter, by tuning the interlayer coupling and magnetization, we construct a topological phase diagram with direct mappings to 3D $\text{MnBi}_2\text{Te}_4/(\text{Bi}_2\text{Te}_3)_n$ compounds, of which the surface AHC features are comprehensively studied. Instead of using over-simplified models, we construct atomistic Hamiltonians from density-functional theory (DFT) with close reliance on realistic attributes of materials, yielding a direct comparison with the angle-resolved

photoemission spectroscopy (ARPES) measurements for the band dispersions. By projecting the Chern number of a thick slab onto each VdW layer, we find that such real-space, local Chern marker in the axion insulator phase is well localized at the surface and results in a surface AHC either saturated at or oscillating around $e^2/2h$, depending on the magnetic homogeneity. In addition, while both the axion insulator and 3D Chern insulator phase can be characterized by the symmetry indicator of inversion $\mathbb{Z}_4 = 2$, the latter, as well as Weyl semimetal phase, do not manifest a well-defined surface AHC. Therefore, the locality of the surface AHC is determined by the chiral side surface states of the bulk, rather than the metallicity of the bulk or slab. Finally, we discuss the preconditions and several experimental proposals to reveal the half-quantized surface AHC in $\text{MnBi}_2\text{Te}_4/(\text{Bi}_2\text{Te}_3)_n$.

Multiple topological phases in $\text{MnBi}_2\text{Te}_4/(\text{Bi}_2\text{Te}_3)$

To begin with, we tune the hopping parameter between VdW layers in $\text{MnBi}_2\text{Te}_4/(\text{Bi}_2\text{Te}_3)_n$ to realize different 3D topological phases, and illustrate that a well-localized, half-quantized surface AHC is the signature of the axion insulator phase. Recall that a MnBi_2Te_4 monolayer can be effectively described by a Bi_2Te_3 monolayer under a ferromagnetic (FM) exchange field [24], we consider a 3D layered structure composed by vertically stacking 2D TIs, *i.e.*, bilayer Bi_2Te_3 , with variable separation between bilayers (d) and magnetization (M). Thanks to the successful synthesis of single-crystal Mn-Bi-Te family and molecular beam epitaxy technique, such multilayer heterostructure could be realized by intercalating an atomic or VdW buffer layer, *e.g.*, BN or In_2Se_3 , into $\text{MnBi}_2\text{Te}_4/(\text{Bi}_2\text{Te}_3)_n$. The model Hamiltonian is written as

$$H = \hbar v_f \tau_z (\boldsymbol{\sigma} \times \mathbf{k})_z + m_k \tau_x + M \sigma_z + t_{IB}^0 (v_+ \tau_- + v_- \tau_+) + t_{IB} (v_+ \tau_+ e^{ik_z D} + v_- \tau_- e^{-ik_z D}), \quad (1)$$

where $\mathbf{k} = (k_x, k_y, k_z) = (k_{\parallel}, k_z)$ is the momentum, σ , τ and v are Pauli matrices acting on spin, surface and layer, respectively [26], with $s_{\pm} = (s_x \pm i s_y)/2$, ($s = \tau, v$). The first two terms describe a monolayer Bi_2Te_3 with Fermi velocity v_f and Dirac mass $m_k = (\Delta - B k_{\parallel}^2)$ [27,28], while the third term denotes the FM exchange coupling between the magnetization M and electrons' spin. Intra-bilayer and inter-bilayer tunneling are considered as the k_z -independent hopping and k_z -dependent hopping in the last two terms with t_{IB}^0 the intra-bilayer hopping integral and D the superlattice period. For the inter-bilayer hopping, we introduce an

exponentially decaying scaling, i.e., $t_{IB} = t_{IB}^0 \cdot e^{-\alpha(d-d_0)/d_0}$, where d_0 and d are the intra- and inter-bilayer spacing. The analytical solutions of Eq. (1) is provided in Supplemental Material [29].

As shown in Fig. 1(a), the origin of the phase diagram represents a 3D Bi_2Te_3 TI phase. Varying the inter-bilayer coupling with preserved T leads to a \mathbb{Z}_2 classification, denoted by the horizontal axis. When the inter-bilayer coupling is weakened, the phase transition between strong TI ($\mathbb{Z}_2 = 1$) and weak TI ($\mathbb{Z}_2 = 0$) occurs. With increasing magnetization, the two TI phases evolve to axion insulator and 3D fragile QSH insulator, respectively, the latter of which can be considered as a trivial stacking of T -broken QSH insulator [30]. When the exchange field is strong enough, a 3D Chern insulator phase [31-33] with chiral side surface states emerges. Under a finite exchange field, the transition between these three topologically distinct insulating phases inevitably passes an intermediate region, i.e., the Weyl semimetal phase [34].

Depending on the magnetization per VdW layer, the different pristine FM $\text{MnBi}_2\text{Te}_4/(\text{Bi}_2\text{Te}_3)_n$ compounds can be mapped onto the vertical axis of the phase diagram with $d=d_0$, as marked by the red stars in Fig. 1(a). Since the Hamiltonian in Eq. (1) has I , one can compute the symmetry indicator of I , a \mathbb{Z}_4 invariant, to determine their topological nature [35-38]:

$$\mathbb{Z}_4 = \sum_{k=1}^8 \frac{n_k^+ - n_k^-}{2} \text{ mod } 4, \quad (2)$$

where n_k^+/n_k^- is the number of occupied states with even/odd parity at one of the eight inversion-invariant momenta \mathbf{k} . By adding a small magnetization, each doubly-degenerate band of the strong TI and weak TI phases splits into two bands with the same parity, leading to $\mathbb{Z}_4 = 2$ and $\mathbb{Z}_4 = 0$, respectively. Although the latter case, i.e., 3D fragile QSH insulator, has a trivial \mathbb{Z}_4 invariant, it leads to a distinct type of “fragile topology”, manifesting a novel twisted bulk-boundary correspondence [39,40]. For the 3D Chern insulator which is adiabatically connected to a vertical stacking of a series of 2D Chern insulators, it also yields $\mathbb{Z}_4 = 2$, but from a different parity distribution compared with the axion insulator. As shown in Fig. 1(a), T symmetry is always broken at a generic point in the phase diagram except for the horizontal line with $M = 0$, which implies that any transition between two of the three insulating phases must be connected by an intermediate Weyl-semimetal phase. Our symmetry analysis based on DFT calculations show that all the pristine FM $\text{MnBi}_2\text{Te}_4/(\text{Bi}_2\text{Te}_3)_n$ ($n = 1-4$) compounds are I -preserved axion

insulators. For comparison, we also calculate $\text{Mn}_2\text{Bi}_2\text{Te}_5$ where the magnetic moments per VdW layer is twice as that in MnBi_2Te_4 , and obtain an unambiguous Weyl semimetal phase, as marked in Fig.1(a).

Half-quantized surface AHC in $\text{MnBi}_2\text{Te}_4/(\text{Bi}_2\text{Te}_3)_n$ axion insulators

Having established the phase diagram, we next calculate the profile of the local Chern marker [41] of the topological phases with nontrivial \mathbb{Z}_4 numbers. In principle, one can define a local AHC $\sigma_{AHC} = C_z \cdot \frac{e^2}{h}$, with C_z being the real-space projected Chern number in the z direction. Using realistic tight-binding Hamiltonians in the Wannier-function basis transformed from the Bloch eigenstates obtained by DFT calculations, we compute the local Chern marker $C_z(l)$ projected onto each VdW layer [42,43], expressed as

$$C_z(l) = \frac{-4\pi}{A} \text{Im} \frac{1}{N_k} \sum_k \sum_{vv'c} X_{vck} Y_{v'ck}^\dagger \rho_{vv'k}(l), \quad (3)$$

where X and Y are the velocity operators along the x and y directions, respectively. $\rho_{vv'k}(l)$ is the projection matrix on to the corresponding layer l , which implies a summation over all atoms within a VdW layer. Details of the calculations are provided in the Supplemental Material [29].

The results for the pristine FM MnBi_2Te_4 slabs are shown in Fig. 1(b). We find that the integrated layer-projected Chern marker $\mathbb{C}(l) = \sum_l C_z(l)$ is stabilized at 1/2 for $l > 2$, and rises up to 1 when it passes over the last two layers, giving rise to a Chern insulator as a whole with $\mathbb{C} = 1$. In this sense, the penetration depth of the surface AHC is about two SLs, while the internal layers do not contribute to the AHC due to the homogeneous spin alignment. Such behavior is similar to the prediction of the axion insulator phase in a nonmagnetic bulk TI with gapped surface [5]. In addition, the slabs with more than 4 SLs are thick enough to reveal the half quantization localized at the top two SLs, indicating an I -preserved, FM axion insulator phase regardless of the thickness of the whole slab.

The FM MnBi_2Te_4 turns into a 3D Chern insulator when $d \geq 1.7d_0$, for which the Chern number of a 2D slice within the k_x - k_y plane at an arbitrary k_z equals to 1 [29]. Despite sharing the same \mathbb{Z}_4 invariant with the axion insulator, $\mathbb{C}(l)$ of the 3D Chern insulator behaves quite differently. As shown in Fig. 1(c), each bilayer contributes to an exact quantized Chern number 1,

giving rise to a $\mathbb{C}(l)$ proportional to l . Therefore, there is no well-defined surface AHC, instead the total AHC of the slab is proportional to the total number of primitive cells in the slab.

We note in Fig. 1(a) that bulk FM MnBi_2Te_4 falls in the vicinity of the boundary between axion insulator and Weyl semimetal [34], which is thus sensitive to numerical details such as the choice of exchange-correlation functionals and lattice constants [21,23]. Fig. 1(d) shows the corresponding $\mathbb{C}(l)$ for the Weyl semimetal phase obtained by applying a 1% lattice expansion. It is found that for the insulating slabs [29], the surface AHC is no longer quantized to $1/2$ due to the bulk contribution. Especially for the slabs thicker than five VdW layers, the surface AHC contribution from the top and bottom two layers ranges from 0.42 to 0.35, while the internal-layer contribution increases linearly with the number of layers due to the bulk AHC [44]. For all these slabs, the distribution of the $e^2/2h$ AHC is not localized at one surface but extends to the center of the slab.

We now focus on the axion insulator phase and its surface AHC in $\text{MnBi}_2\text{Te}_4/(\text{Bi}_2\text{Te}_3)_n$ compounds. The magnetic ground states for MnBi_2Te_4 , MnBi_4Te_7 and $\text{MnBi}_6\text{Te}_{10}$ ($n = 0-2$) are A-type AFM along the z axis with the local moments of Mn ordered ferromagnetically within each MnBi_2Te_4 layer [16,45]; while $\text{MnBi}_8\text{Te}_{13}$ ($n = 3$) is a ferromagnet [18]. From the perspective of \mathbb{Z}_4 indices, all of the abovementioned compounds, no matter FM or AFM states, are I -preserved axion insulators according to our DFT calculations. Compared with FM MnBi_2Te_4 , the topmost layer of the AFM phase contributes almost half-quantized AHC, i.e., $C_z(1) = 0.49$, while the bottom layer contributes an opposite AHC $C_z(16) = -0.49$, achieving a zero Hall plateau state with the total Chern number to be zero. Starting from the second layer, $\mathbb{C}(l)$ no longer saturates but oscillates around $1/2$ with a period of the unit cell in the z direction, i.e., two VdW layers. Every additional layer contributes reversely to σ_{AHC} due to the flipping spin direction, leading to the oscillation with the amplitude as large as $0.21e^2/h$. Such behavior is in sharp contrast to T -preserved axion insulators proposed before. For the case of FM and AFM MnBi_4Te_7 , the layer-projected AHC at MnBi_2Te_4 termination reaches the half-quantized value after three or four VdW layers, then oscillates around $e^2/2h$, again, due to the inhomogeneity of the magnetic moments. The oscillation period is also determined by the thickness of a unit cell, i.e., 2 (4) VdW layers for FM (AFM) phase.

It is worthwhile to note that the half-quantized AHC of an axion insulator is a local property at the gapped surface [46]. To demonstrate this, we consider a thick slab of FM MnBi_4Te_7 , which is insulating for the MnBi_2Te_4 termination but metallic for the Bi_2Te_3 termination. We find that as long as the Fermi level (E_f) locates within the surface gap of the MnBi_2Te_4 termination, the corresponding surface AHC would stay around $e^2/2h$. On the other hand, the surface AHC with the metallic Bi_2Te_3 termination varies with different choices of E_f , with the details provided in Supplemental Material [29].

Experimental realization

We next discuss the experimental prerequisites and signatures of the half-quantized surface AHC in $\text{MnBi}_2\text{Te}_4/(\text{Bi}_2\text{Te}_3)_n$. First of all, a gapped surface state of an axion insulator is the kernel to realize the half quantization effect. Figs. 3(a) and 3(b) provide the direct comparison of our ARPES and DFT results, from which we can distinguish two different types of surface gaps in $\text{MnBi}_2\text{Te}_4/(\text{Bi}_2\text{Te}_3)_n$ depending on the specific terminations. Type I originates from the typical surface magnetization that introduces a $M_z\sigma_z$ term to a gapless Dirac fermion, exemplified by the (001) surface of MnBi_2Te_4 , and the MnBi_2Te_4 -termination of $\text{MnBi}_2\text{Te}_4/(\text{Bi}_2\text{Te}_3)_n$. We note that although the surface states of MnBi_2Te_4 are reported to be gapless due to the possible reconstruction of the geometric or magnetic configurations at the surface [47-49], there are still unambiguous surface gaps observed in various conditions including Sb-doped MnBi_2Te_4 and the MnBi_2Te_4 -termination of $\text{MnBi}_8\text{Te}_{13}$ [50-52]. Type II, on the other hand, is caused by the hybridization effect between the upper Dirac cone and the bulk valence band, exemplified by the Bi_2Te_3 -termination of MnBi_4Te_7 [53]. Compared with the magnetization gap, the hybridization gap exchanges the orbital characters of the surface band and bulk band. Nevertheless, the broken T also gives rise to imbalance Berry curvature with opposite momenta and thus a half-quantized AHC, with the details provided in Supplemental Material [29].

One might wonder what kind of “mode” carries the half-quantized AHC in a realistic material, because ordinarily a hinge state carries, if any, an integer number of chiral modes when the two connecting surfaces are both gapped. In $\text{MnBi}_2\text{Te}_4/(\text{Bi}_2\text{Te}_3)_n$ compounds with Mn moments along the z direction, the AFM phase manifests a gapless Dirac cone at the side surface due to the combined symmetry between T and the half-cell translation [54], while for the FM phase the side surface could be slightly gapped by the magnetization and a lower crystal symmetry [see

Figs. 4(a) and 4(b)]. Such a gap, stemming from a high-order effect of spin-momentum locking, is much smaller than that at the top-surface gap and can be neglected as long as the chemical potential lies outside the side-surface gap. Similar to the nonmagnetic TI, the manifestation of the bulk magnetoelectric response at the side surface, *i.e.*, $e^2/2h$ AHC, is compensated by the opposite contribution from the surface Dirac cone, leaving a half-quantized AHC only from the top surface. Fig. 4c shows the local density of states of the hinge state of MnBi_2Te_4 formed by the gapped top surface (xy) and a gapless side surface (xz) [29]. In this spectrum there is a chiral mode embedded into the gapless side surface, giving rise to half-quantized AHC in total. Therefore, considering a thick-enough sample with the multi-terminal leads attached to one surface covering only a few VdW layer, one can expect the conductance plateau of $e^2/2h$ without magnetic fields through Hall or nonlocal measurements [55] [see Fig. 4(e)].

A chiral boundary modes with integer AHC could also be detected at the magnetic domain wall at the surface of $\text{MnBi}_2\text{Te}_4/(\text{Bi}_2\text{Te}_3)_n$ as the evidence of half quantization. Domains with opposite magnetization on the surface can be effectively controlled using magnetic force microscopy. Previous experiments on thin films of magnetic TI $\text{Cr}_x(\text{Bi}_{1-y}\text{Sb}_y)_{2-x}$ resulted in dual edge modes with a step change in Chern number $\Delta C = 2$ at the domain wall, manifesting the Chern numbers $C = \pm 1$ for each domain [56]. In stoichiometric $\text{MnBi}_2\text{Te}_4/(\text{Bi}_2\text{Te}_3)_n$, on the other hand, the surface states from the opposite surfaces could be significantly decoupled by fabricating thick samples. We consider an effective surface Hamiltonian with a domain wall extending along the x axis: $H(x, y) = -iv(\partial_y\sigma_x - \partial_x\sigma_y) - \text{sgn}(y)M_z\sigma_z$. Such a Hamiltonian hosts a single chiral eigenmode with linear dispersion $E = vk_x$ localized at the domain wall as shown in Fig. 4(d), indicating a discontinuous change $\Delta C = 1$. Since the two domains are related by time-reversal operation, this single chiral mode indicates the opposite surface Chern number $\pm 1/2$ for each domain. Furthermore, measurable chiral state can also appear in the hinge of a geometrically designed sample, as an equivalent manifestation of high-order topology [57,58]. By cutting a FM $\text{MnBi}_2\text{Te}_4/(\text{Bi}_2\text{Te}_3)_n$ sample into a wedge shape, as sketched in Fig. 4(e), we achieve a fully gapped magnetic TI while the top surface state has an opposite half-quantized Chern number in comparison to other surface states. This leads to a chiral mode with e^2/h AHC at the hinges of the top surface.

To summarize, we construct a $\text{MnBi}_2\text{Te}_4/(\text{Bi}_2\text{Te}_3)_n$ -based phase diagram with various 3D topological states, including axion insulators, 3D Chern insulators, 3D fragile QSH insulators and Weyl semimetals. While the axion insulator phase cannot be fully characterized by $\mathbb{Z}_4 = 2$, it manifests a surface AHC saturated at or oscillates around $e^2/2h$. The locality of the surface AHC does not rely on the metallicity of the whole slab, but the zero contribution of the local Chern marker from the bulk state, i.e., $\sum_{l \in \text{internal}}^{l+u.c.} C(l) = 0$. Our finding establishes an ideal platform to realize the half-quantized AHC and the related topological magnetoelectric phenomena, paving new and accessible avenues within the long-sought axion states in condensed matter systems.

Acknowledgements

We thank Haizhou Lu, Ni Ni, Zhida Song and Zhongjia Chen for helpful discussions. This work was supported by the National Natural Science Foundation of China under Grant No. 11874195, National Key R&D Program of China under Grant No. 2019YFA0704904, Guangdong Innovative and Entrepreneurial Research Team Program under Grant No. 2017ZT07C062. and Guangdong Provincial Key Laboratory for Computational Science and Material Design under Grant No. 2019B030301001 and Center for Computational Science and Engineering of Southern University of Science and Technology.

References

- [1] X.-L. Qi, T. L. Hughes, and S.-C. Zhang, Topological field theory of time-reversal invariant insulators, *Phys. Rev. B* **78**, 195424 (2008).
- [2] A. M. Essin, J. E. Moore, and D. Vanderbilt, Magnetoelectric Polarizability and Axion Electrostatics in Crystalline Insulators, *Phys. Rev. Lett.* **102**, 146805 (2009).
- [3] L. Fu and C. L. Kane, Topological insulators with inversion symmetry, *Phys. Rev. B* **76**, 045302 (2007).
- [4] X.-L. Qi, R. Li, J. Zang, and S.-C. Zhang, Inducing a Magnetic Monopole with Topological Surface States, *Science* **323**, 1184 (2009).
- [5] N. P. Armitage and L. Wu, On the matter of topological insulators as magnetoelectrics, *SciPost Physics* **6**, 046 (2019).
- [6] M. Mogi, M. Kawamura, R. Yoshimi, A. Tsukazaki, Y. Kozuka, N. Shirakawa, K. S. Takahashi, M. Kawasaki, and Y. Tokura, A magnetic heterostructure of topological insulators as a candidate for an axion insulator, *Nat. Mater.* **16**, 516 (2017).
- [7] M. Mogi, M. Kawamura, A. Tsukazaki, R. Yoshimi, K. S. Takahashi, M. Kawasaki, and Y. Tokura, Tailoring tricolor structure of magnetic topological insulator for robust axion insulator, *Sci. Adv.* **3**, eaao1669 (2017).
- [8] M. Allen, Y. Cui, E. Y. Ma, M. Mogi, M. Kawamura, I. C. Fulga, D. Goldhaber-Gordon, Y. Tokura, and Z.-X. Shen, Visualization of an axion insulating state at the transition between 2 chiral quantum anomalous Hall states, *Proc. Natl. Acad. Sci. U.S.A.* **116**, 14511 (2019).
- [9] D. Xiao *et al.*, Realization of the Axion Insulator State in Quantum Anomalous Hall Sandwich Heterostructures, *Phys. Rev. Lett.* **120**, 056801 (2018).
- [10] J. Wang, B. Lian, X.-L. Qi, and S.-C. Zhang, Quantized topological magnetoelectric effect of the zero-plateau quantum anomalous Hall state, *Phys. Rev. B* **92**, 081107 (2015).
- [11] E. J. Koenig, P. M. Ostrovsky, I. V. Protopopov, I. V. Gornyi, I. S. Burmistrov, and A. D. Mirlin, Half-integer quantum Hall effect of disordered Dirac fermions at a topological insulator surface, *Phys. Rev. B* **90**, 165435 (2014).
- [12] R.-L. Chu, J. Shi, and S.-Q. Shen, Surface edge state and half-quantized Hall conductance in topological insulators, *Phys. Rev. B* **84**, 085312 (2011).
- [13] M. M. Otrokov *et al.*, Prediction and observation of an antiferromagnetic topological insulator, *Nature* **576**, 416 (2019).

- [14] E. D. L. Rienks *et al.*, Large magnetic gap at the Dirac point in Bi₂Te₃/MnBi₂Te₄ heterostructures, *Nature* **576**, 423 (2019).
- [15] Y. Gong *et al.*, Experimental Realization of an Intrinsic Magnetic Topological Insulator, *Chin. Phys. Lett.* **36**, 076801 (2019).
- [16] C. Hu *et al.*, A van der Waals antiferromagnetic topological insulator with weak interlayer magnetic coupling, *Nat. Commun.* **11**, 97 (2020).
- [17] K. N. Gordon *et al.*, Strongly Gapped Topological Surface States on Protected Surfaces of Antiferromagnetic MnBi₄Te₇ and MnBi₆Te₁₀, arXiv, 1910.13943 (2019).
- [18] C. Hu *et al.*, Realization of an intrinsic, ferromagnetic axion insulator in MnBi₈Te₁₃, arXiv, 1910.12847 (2019).
- [19] Y. Deng, Y. Yu, M. Z. Shi, Z. Guo, Z. Xu, J. Wang, X. H. Chen, and Y. Zhang, Quantum anomalous Hall effect in intrinsic magnetic topological insulator MnBi₂Te₄, *Science* **367**, 895 (2020).
- [20] C. Liu *et al.*, Robust axion insulator and Chern insulator phases in a two-dimensional antiferromagnetic topological insulator, *Nat. Mater.* **19**, 522 (2020).
- [21] D. Zhang, M. Shi, T. Zhu, D. Xing, H. Zhang, and J. Wang, Topological Axion States in the Magnetic Insulator MnBi₂Te₄ with the Quantized Magnetoelectric Effect, *Phys. Rev. Lett.* **122**, 206401 (2019).
- [22] J. Li, Y. Li, S. Du, Z. Wang, B.-L. Gu, S.-C. Zhang, K. He, W. Duan, and Y. Xu, Intrinsic magnetic topological insulators in van der Waals layered MnBi₂Te₄-family materials, *Sci. Adv.* **5**, eaaw5685 (2019).
- [23] J. Ge, Y. Liu, J. Li, H. Li, T. Luo, Y. Wu, Y. Xu, and J. Wang, High-Chern-Number and High-Temperature Quantum Hall Effect without Landau Levels, arXiv, 1907.09947 (2019).
- [24] H. Sun *et al.*, Rational Design Principles of the Quantum Anomalous Hall Effect in Superlatticelike Magnetic Topological Insulators, *Phys. Rev. Lett.* **123**, 096401 (2019).
- [25] R.-X. Zhang, F. Wu, and S. Das Sarma, Mⁿ-obius Insulator and Higher-Order Topology in MnBi_{2n}Te_{3n+1}, *Phys. Rev. Lett.* **124**, 136407 (2020).
- [26] Note that here "surface" refers to the two surface states of each TI monolayer, which are coupled together by the hybridization term $m_k \tau_z$, with $m_k = (\Delta - Bk_{\parallel}^2)$.
- [27] B. A. Bernevig, T. L. Hughes, and S.-C. Zhang, Quantum Spin Hall Effect and Topological Phase Transition in HgTe Quantum Wells, *Science* **314**, 1757 (2006).

- [28] H.-Z. Lu, A. Zhao, and S.-Q. Shen, Quantum Transport in Magnetic Topological Insulator Thin Films, *Phys. Rev. Lett.* **111**, 146802 (2013).
- [29] See Supplemental Material at <http://> for k·p model of the multilayer topological heterostructure, methods of DFT calculations and the local Chern marker, electronic structures of different topological phases in MnBi₂Te₄, locality of the half-quantized surface AHC, two different types of surface gaps in MnBi₂Te₄/(Bi₂Te₃)_n, and calculations of the surface state and chiral hinge state.
- [30] Y. Yang, Z. Xu, L. Sheng, B. Wang, D. Y. Xing, and D. N. Sheng, Time-Reversal-Symmetry-Broken Quantum Spin Hall Effect, *Phys. Rev. Lett.* **107**, 066602 (2011).
- [31] B. I. Halperin, Possible States for a Three-Dimensional Electron Gas in a Strong Magnetic Field, *Jpn. J. Appl. Phys.* **26**, 1913 (1987).
- [32] B. A. Bernevig, T. L. Hughes, S. Raghu, and D. P. Arovas, Theory of the three-dimensional quantum hall effect in graphite, *Phys. Rev. Lett.* **99**, 146804 (2007).
- [33] Y. J. Jin, R. Wang, B. W. Xia, B. B. Zheng, and H. Xu, Three-dimensional quantum anomalous Hall effect in ferromagnetic insulators, *Phys. Rev. B* **98**, 081101 (2018).
- [34] A. A. Burkov and L. Balents, Weyl Semimetal in a Topological Insulator Multilayer, *Phys. Rev. Lett.* **107**, 127205 (2011).
- [35] J. Kruthoff, J. de Boer, J. van Wezel, C. L. Kane, and R.-J. Slager, Topological Classification of Crystalline Insulators through Band Structure Combinatorics, *Phys. Rev. X* **7**, 041069 (2017).
- [36] H. Watanabe, H. C. Po, and A. Vishwanath, Structure and topology of band structures in the 1651 magnetic space groups, *Sci. Adv.* **4**, eaat8685 (2018).
- [37] S. Ono and H. Watanabe, Unified understanding of symmetry indicators for all internal symmetry classes, *Phys. Rev. B* **98**, 115150 (2018).
- [38] Y. Xu, Z. Song, Z. Wang, H. Weng, and X. Dai, Higher-Order Topology of the Axion Insulator EuIn₂As₂, *Phys. Rev. Lett.* **122**, 256402 (2019).
- [39] H. C. Po, H. Watanabe, and A. Vishwanath, Fragile Topology and Wannier Obstructions, *Phys. Rev. Lett.* **121**, 126402 (2018).
- [40] Z.-D. Song, L. Elcoro, and B. A. Bernevig, Twisted bulk-boundary correspondence of fragile topology, *Science* **367**, 794 (2020).

- [41] R. Bianco and R. Resta, Mapping topological order in coordinate space, *Phys. Rev. B* **84**, 241106 (2011).
- [42] T. Rauch, T. Olsen, D. Vanderbilt, and I. Souza, Geometric and nongeometric contributions to the surface anomalous Hall conductivity, *Phys. Rev. B* **98**, 115108 (2018).
- [43] N. Varnava and D. Vanderbilt, Surfaces of axion insulators, *Phys. Rev. B* **98**, 245117 (2018).
- [44] X. Wan, A. M. Turner, A. Vishwanath, and S. Y. Savrasov, Topological semimetal and Fermi-arc surface states in the electronic structure of pyrochlore iridates, *Phys. Rev. B* **83**, 205101 (2011).
- [45] J. Q. Yan *et al.*, Crystal growth and magnetic structure of MnBi_2Te_4 , *Phys. Rev. Mater.* **3**, 064202 (2019).
- [46] A. Marrazzo and R. Resta, Locality of the anomalous Hall conductivity, *Phys. Rev. B* **95**, 121114 (2017).
- [47] Y.-J. Hao *et al.*, Gapless Surface Dirac Cone in Antiferromagnetic Topological Insulator MnBi_2Te_4 , *Phys. Rev. X* **9**, 041038 (2019).
- [48] H. Li *et al.*, Dirac Surface States in Intrinsic Magnetic Topological Insulators EuSn_2As_2 and $\text{MnBi}_{2n}\text{Te}_{3n+1}$, *Phys. Rev. X* **9**, 041039 (2019).
- [49] Y. J. Chen *et al.*, Topological Electronic Structure and Its Temperature Evolution in Antiferromagnetic Topological Insulator MnBi_2Te_4 , *Phys. Rev. X* **9**, 041040 (2019).
- [50] X.-M. Ma *et al.*, Spectroscopic realization of large surface gap in a doped magnetic topological insulator, arXiv, 2004.09123 (2020).
- [51] R. Lu *et al.*, Unpublished work.
- [52] A. M. Shikin *et al.*, Nature of the Dirac gap modulation and surface magnetic interaction in axion antiferromagnetic topological insulator MnBi_2Te_4 , arXiv, arXiv:2004.04802 (2020).
- [53] X. Wu *et al.*, Distinct Topological Surface States on the Two Terminations of MnBi_4Te_7 , arXiv, 2002.00320 (2020).
- [54] R. S. K. Mong, A. M. Essin, and J. E. Moore, Antiferromagnetic topological insulators, *Phys. Rev. B* **81**, 245209 (2010).
- [55] R. Chen, S. Li, H.-P. Sun, H.-Z. Lu, and X. C. Xie, Using nonlocal surface transport to identify the axion insulator, arXiv, 2005.14074 (2020).

- [56] K. Yasuda, M. Mogi, R. Yoshimi, A. Tsukazaki, K. S. Takahashi, M. Kawasaki, F. Kagawa, and Y. Tokura, Quantized chiral edge conduction on domain walls of a magnetic topological insulator, *Science* **358**, 1311 (2017).
- [57] E. Khalaf, Higher-order topological insulators and superconductors protected by inversion symmetry, *Phys. Rev. B* **97**, 205136 (2018).
- [58] N. Okuma, M. Sato, and K. Shiozaki, Topological classification under nonmagnetic and magnetic point group symmetry: Application of real-space Atiyah-Hirzebruch spectral sequence to higher-order topology, *Phys. Rev. B* **99**, 085127 (2019).

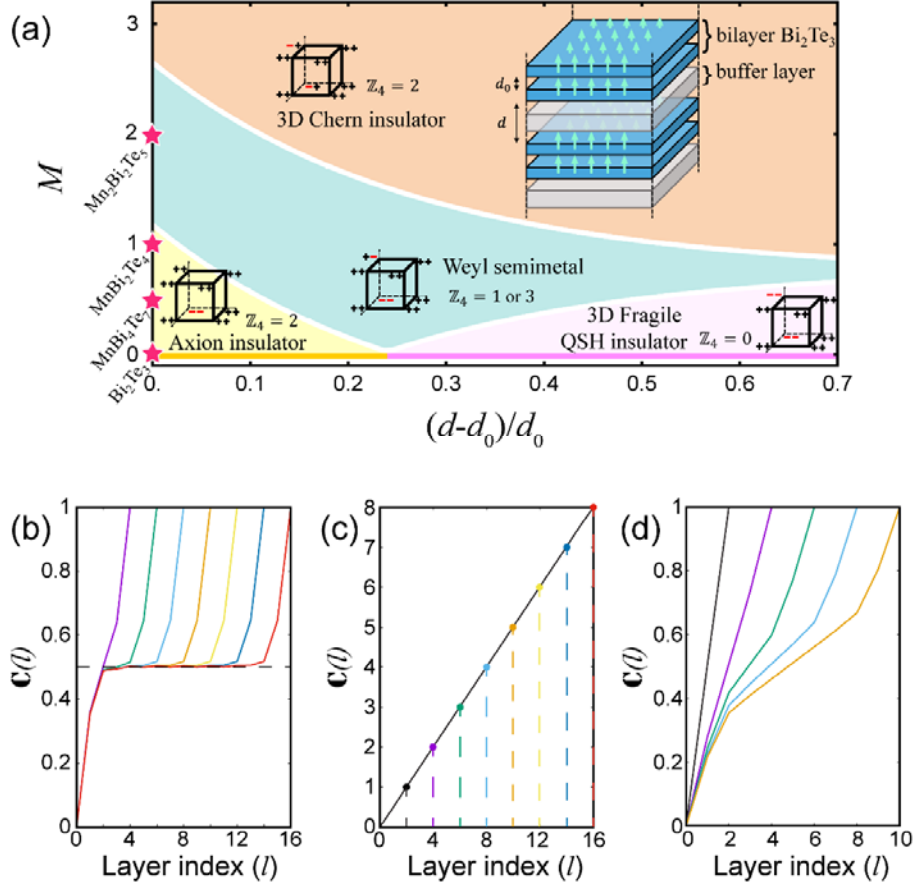


Fig. 1. (a) Phase diagram of the multilayer topological heterostructure in terms of relative spacing $(d - d_0)/d_0$ and magnetization M (rescaled as the number of Mn layers per VdW layer). Insets show the sketch of the heterostructure and \mathbb{Z}_4 indices with parities. Four pristine topological materials in FM phase Bi₂Te₃ ($M = 0$), MnBi₄Te₇ ($M = 1/2$), MnBi₂Te₄ ($M = 1$) and Mn₂Bi₂Te₅ ($M = 2$) are mapped at the vertical axis. (b-d) Integrated local Chern marker $\mathcal{C}(l)$ for MnBi₂Te₄ slabs in (a) axion insulator, (b) Weyl semimetal, and (c) 3D Chern insulator phases. Different colors denote slabs with different thickness.

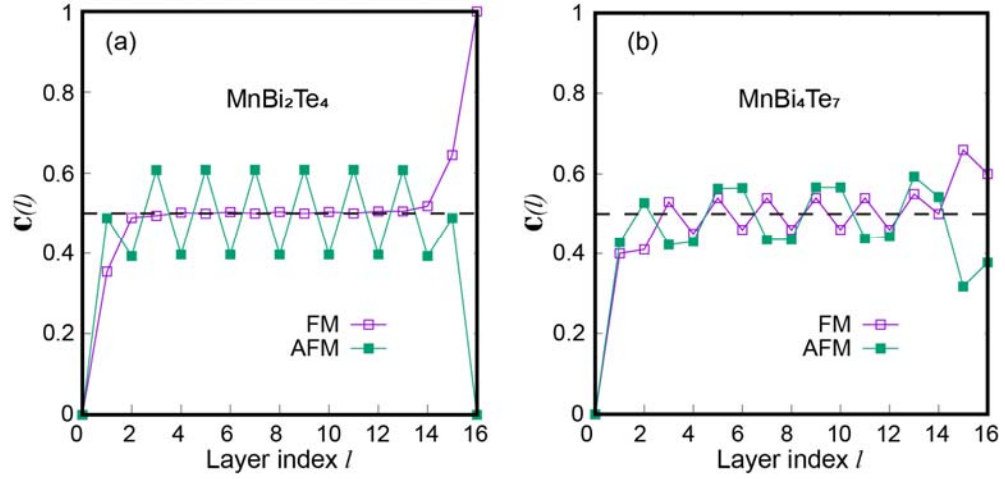


Fig. 2: (a-b) Integrated local Chern marker $\mathbb{C}(l)$ as a function of layer index l for a 16-layer slab of (a) MnBi_2Te_4 and (b) MnBi_4Te_7 .

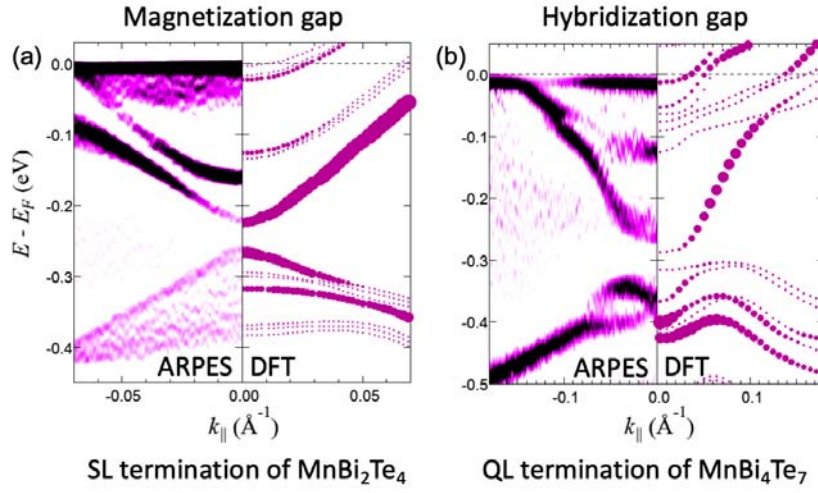


Fig. 3: Comparison of band structures between ARPES and DFT results for the (001) surface of (a) MnBi_2Te_4 with slightly Sb doping and (b) the Bi_2Te_3 -termination of MnBi_4Te_7 .

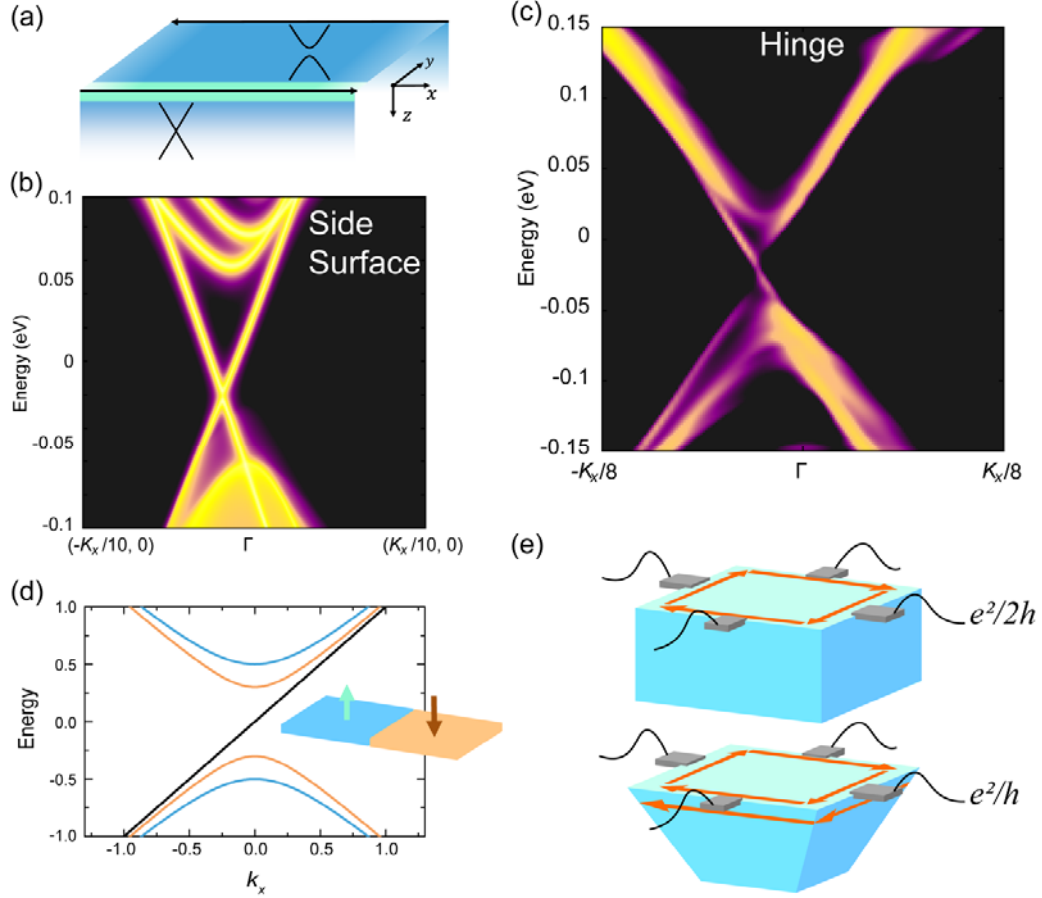


Fig. 4: (a) Schematic plot of the hinge state of MnBi₂Te₄/(Bi₂Te₃)_n at the gapped top surface (xy). Local density of states of (b) the gapless side surface state (xz) and (c) the hinge state marked in panel (a), showing a chiral mode embedded into the Dirac cone of the side surface. (d) Energy spectrum with a single chiral mode at the surface of MnBi₂Te₄/(Bi₂Te₃)_n with a magnetic domain wall. (e) Schematic drawing of two devices of MnBi₂Te₄/(Bi₂Te₃)_n. The multi-terminal transport measurements with the leads attached at one surface could give rise to half-quantized and integer-quantized AHC for an ordinary and a wedge-shaped device, respectively.